nature photonics

Supplementary information

https://doi.org/10.1038/s41566-024-01495-y

An 8×160 Gb s^{-1} all-silicon avalanche photodiode chip

In the format provided by the authors and unedited

Double-MRR RX with “Z” shape doping profile

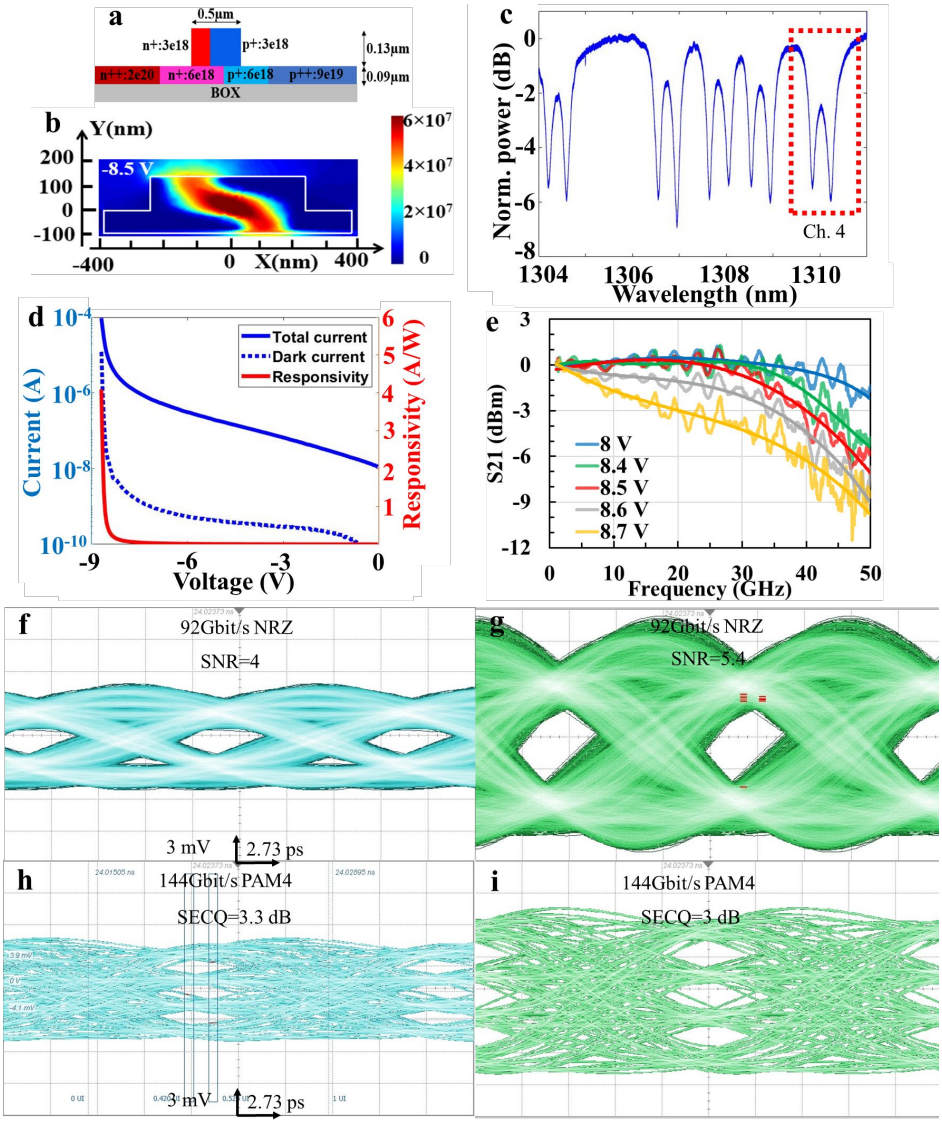

Supplementary Fig. 1. (a) Schematic cross section of “Z” shape doping profile. (b) Simulated electric field of the junction. (c) Normalized transmission spectrum for the 4-channel “Z” shape doped RX. (d) Measured total and dark current. (e) Measured frequency response. Measured 92 Gb/s eye diagrams (f) without FFE and (g) with FFE. Measured 144 Gb/s eye diagrams (h) without FFE and (i) with FFE.

Compared to the conventional APDs [1,2], the main limitation of the all-Si APD is the weak absorption mechanisms. To enhance the light absorption, we also developed a novel “Z” shape PN junction, which is created with two heavy P and N doping concentration of 6×10^{18} cm^{-3} and two light P and N doping concentration of 3×10^{18} cm^{-3}. With the presence of the new doping profile, the junction interface enables a better overlap by ~35% between the high electric field and the optical mode and improve the absorption probability according to simulation [3]. Supplementary Fig. 1b shows the simulated electric field distribution at -8.5 V in the junction, where the PAT effect can induce non-negligible photocurrent with the narrower junction barrier. We prove the feasibility of the all-Si double-MRR RX in a standard Si photonics process at the Advanced Micro Foundry (AMF). For the “Z” shape design, we only have double-MRR structure with 12 μm radius, which works as a 4-channel RX.

The I-V characteristics are measured at the center resonance wavelength as illustrated in Supplementary Fig. 2d where the solid blue line is the total current, the dash blue line is the dark current, and the solid red line is responsivity. The all-Si APD demonstrates a dark current of only ~ 10 nA when responsivity is 0.6 A/W at -8.5 V. The highest responsivity is ~ 4 A/W at -8.68 V, where the input optical power is -16.5 dBm. As a comparison, the double-MRR APD with PIN junction shows the responsivity of ~0.4 A/W at the same dark current level and the same optical power. The "Z" shape implantation improves the photon absorption and responsivity by more than 30%.

The frequency response of the MRR APD at different bias voltage are shown in Supplementary Fig. 1(e). At -8 V, the APD shows 3 dB bandwidth of > 50 GHz, which is close to the calculated photon lifetime limited bandwidth. The bandwidth decreases to ~ 40 GHz at -8.5 V and ~ 35 GHz at -8.6 V. The bandwidth performance is similar to the PIN structure and is comparable to the conventional Si-Ge APDs.

The eye diagrams of the "Z" shape design was also characterized with PRBS9 signals at -8.5 V without TIA. Due to the high bandwidth, the MRR APD thus can support open eye diagrams of 92 Gb/s NRZ with a signal-to-noise ratio of 4 without FFE and a signal-to-noise ratio of 5.4 with 8-tap FFE. The all-Si MRR APD also has sufficient bandwidth and amplitude to support 144 Gb/s PAM4 eye diagrams without equalization with a SECQ penalty of 3.3 dB. With a combination of a third order Bessel filter and an 8-tap feed forward equalizer (FFE), the SECQ penalty decreases to 3 dB. SECQ was measured at a threshold of symbol error rate < 4.8E-4.

In conclusion, the "Z" shape design can improve the absorption and responsivity at the similar frequency response performance for a double-MRR APD. It should be noted that this implantation condition is designed for modulators and is too high for APDs. For the next tapeout with dedicated implantation condition, the 18-channel "Z" shape double-MRR RX will be adopted, and responsivity is estimated to be twice higher.

Analytic Model

Serially and parallel coupled MRR configurations have been described in detail in Chu et al. (1999) [4], Little et al. (1997, 2000) [5,6] and Melloni (2001) [7]. Thus far, there is not much dynamic analysis work to quantify the performance of the coupled MRR APD. To better understand the frequency response, we derived the small-signal response of the MRR APD. We are concerned only with operation near the resonance, the resonator may be modeled using the coupling of modes in time (CMT) approach, which simplifies the small-signal analysis [8]. We view the wave oscillates and travels in resonator with amplitude of $a(t)$, and the $|a(t)|^2$ represents the total energy stored in the MRR. The rate of change for the amplitude in two MRR can expressed as:

$$\frac{da_1}{dt} = (j\omega_r - y_{r1})a_1 - j\mu_2 a_2 - j\mu_1 E_0 \quad (1)$$

$$\frac{da_2}{dt} = (j\omega_r - y_{l2})a_2 - j\mu_2 a_1 \quad (2)$$

where $a_1(t)$ and $a_2(t)$ is the energy amplitude travelling inside the first and second MRR, respectively; ω_r is the resonant angular frequency of the MRR; y_{r1} is the amplitude decay rate in first MRR which consists of a decay rate due to the loss in the resonator y_{l1} and coupling to bus waveguide y_e; y_{l2} is the amplitude decay rate due to loss in the second MRR; E_0 is the input amplitude of waveguide mode; $\mu_1$is the energy coupling coefficient to bus waveguide, which is related to the coupling to bus waveguide y_e and field coupling coefficient k_1: $\mu_1^2 = 2y_e = \frac{k_1^2}{T_{rt}}$; μ_2 is the energy coupling coefficient between MRRs, which is

related to the field coupling coefficient between two MRRs k_2: $\mu_2^2 = \frac{k_2^2}{{T_{rt}}^2}$. T_{rt} is the round-trip transit time in the resonator. The input optical signal consists of a small sinusoidal signal of cos (ω_0t) and an optical carrier of cos ($\omega_m t$), where ω_0 and ω_m are modulation angular frequency and optical carrier frequency. The input optical signal and the energy amplitude can be expressed as:

$$a_1 = a_1^0 e^{j\omega_0 t} + \frac{a_1^+}{2} e^{j(\omega_0+\omega_m)t} + \frac{a_1^-}{2} e^{j(\omega_0-\omega_m)t} \tag{3}$$

$$a_2 = a_2^0 e^{j\omega_0 t} + \frac{a_2^+}{2} e^{j(\omega_0+\omega_m)t} + \frac{a_2^-}{2} e^{j(\omega_0-\omega_m)t} \tag{4}$$

$$E = E^0 e^{j\omega_0 t} + \frac{E^+}{2} e^{j(\omega_0+\omega_m)t} + \frac{E^-}{2} e^{j(\omega_0-\omega_m)t} \tag{5}$$

$a^+$and $a^-$are complex amplitudes of the upper and lower sidebands. In the small-signal regime, where the modulation depth is much less than unity, we can neglect the second-order harmonic that arises from the beating of upper and lower sidebands. Substituting the modulated input and amplitude into Supplementary Eq. (1-2) yield:

$$j\omega_0 a_1^0 e^{j\omega_0 t} + j(\omega_0+\omega_m)\frac{a_1^+}{2} e^{j(\omega_0+\omega_m)t} + j(\omega_0-\omega_m)\frac{a_1^-}{2} e^{j(\omega_0-\omega_m)t} = (j\omega_r - y_{r1}) \cdot (a_1^0 e^{j\omega_0 t} + \frac{a_1^+}{2} e^{j(\omega_0+\omega_m)t} + \frac{a_1^-}{2} e^{j(\omega_0-\omega_m)t}) - j\mu_2 (a_2^0 e^{j\omega_0 t} + \frac{a_2^+}{2} e^{j(\omega_0+\omega_m)t} + \frac{a_2^-}{2} e^{j(\omega_0-\omega_m)t}) - j\mu_1 (E^0 e^{j\omega_0 t} + \frac{E^+}{2} e^{j(\omega_0+\omega_m)t} + \frac{E^-}{2} e^{j(\omega_0-\omega_m)t}) \tag{6}$$

$$j\omega_0 a_2^0 e^{j\omega_0 t} + j(\omega_0+\omega_m)\frac{a_2^+}{2} e^{j(\omega_0+\omega_m)t} + j(\omega_0-\omega_m)\frac{a_2^-}{2} e^{j(\omega_0-\omega_m)t} = (j\omega_r - y_{l2}) \cdot (a_2^0 e^{j\omega_0 t} + \frac{a_2^+}{2} e^{j(\omega_0+\omega_m)t} + \frac{a_2^-}{2} e^{j(\omega_0-\omega_m)t}) - j\mu_2 (a_1^0 e^{j\omega_0 t} + \frac{a_1^+}{2} e^{j(\omega_0+\omega_m)t} + \frac{a_1^-}{2} e^{j(\omega_0-\omega_m)t}) \tag{7}$$

By equating terms at the same frequency, neglecting higher order oscillation terms and cancelling the exponential factors, the equation can be separated into three equations sets:

$$\begin{cases} -(j\Delta\omega + y_{r1})a_1^0 - j\mu_2 a_2^0 - j\mu_1 E^0 = 0 \\ -(j\Delta\omega + y_{l2})a_2^0 - j\mu_2 a_1^0 = 0 \end{cases} \tag{8}$$

$$\begin{cases} j\omega_m a_1^+ = -(j\Delta\omega + y_{r1})a_1^+ - j\mu_2 a_2^+ - j\mu_1 E^+ \\ j\omega_m a_2^+ = -(j\Delta\omega + y_{l2})a_1^+ - j\mu_2 a_1^+ \end{cases} \tag{9}$$

$$\begin{cases} -j\omega_m a_1^- = -(j\Delta\omega + y_{r1})a_1^- - j\mu_2 a_2^- - j\mu_1 E^- \\ -j\omega_m a_2^- = -(j\Delta\omega + y_{l2})a_1^- - j\mu_2 a_1^- \end{cases} \tag{10}$$

where $\Delta\omega = \omega_0 - \omega_r$, is the angular frequency detuning of the input carrier frequency from the resonance frequency. a_2^0 is the steady state amplitude. a_2^0, $a_2^+$and a_2^-can be solved as:

$$a_2^0 = -\frac{\mu_1\mu_2 E^0}{(j\Delta\omega+y_{r1})\cdot(j\Delta\omega+y_{l2})+\mu_2^2} \tag{11}$$

$$a_2^+ = -\frac{\mu_1\mu_2 E^+}{(j\Delta\omega+j\omega_m+y_{r1})\cdot(j\Delta\omega+j\omega_m+y_{l2})+\mu_2^2} \tag{12}$$

$$a_2^- = -\frac{\mu_1\mu_2 E^-}{(j\Delta\omega-j\omega_m+y_{r1})\cdot(j\Delta\omega-j\omega_m+y_{l2})+\mu_2^2} \tag{13}$$

The photocurrent depends on the absorption coefficient, R, and optical power in the resonator. The transfer function from optical power to photocurrent squared can be written as: $H_o = \frac{R}{E_0^2 T_{rt}} |(a_2^0 + a_2^+ + a_2^-)|^2$ and the RF part can be expressed as: $\frac{R}{E_0^2 T_{rt}} Re\{(a_2^{0^*} a_2^+ + a_2^0 a_2^{-^*})\}$. By substituting Supplementary Eq. (11-13), the frequency response can be written as:

$$H_{tran}(\omega_m) = \frac{R\eta_m}{T_{rt}} \cdot \frac{\mu_1^2 \mu_2^2}{y_{r1} y_{l2} + \mu_2^2} \cdot \frac{1}{(j\omega_m + y_{r1}) \cdot (j\omega_m + y_{l2}) + \mu_2^2} \tag{14}$$

When the $\Delta\omega = 0$ (input frequency is at resonance frequency) and this is the working condition for the double-MRR PD. η_m is the modulation depth. As the response has two complex poles and the magnitude of the frequency response show an enhancement at frequencies in the proximity of the two poles, which will introduce the peaking effect for the double-MRR PD bandwidth.

The PD frequency response is also limited by the RC time. The RC constant is >70 GHz for our Si PIN junction as shown in [9], which can be neglected. The single-MRR PD is simulated using the method well described in [10].

The APD bandwidth is also limited by the avalanche buildup time. The avalanche buildup process can be described by a function as:

$$H_{buildup}(\omega_m) = \frac{1}{1 + j\omega_m M \tau_m} \tag{15}$$

where τ_m is the avalanche buildup time and M is the multiplication gain. The detailed information is shown in [11,12]. The overall frequency response would be the product of $H_{tran}(\omega_m)$ and $H_{buildup}(\omega_m)$.

Design considerations

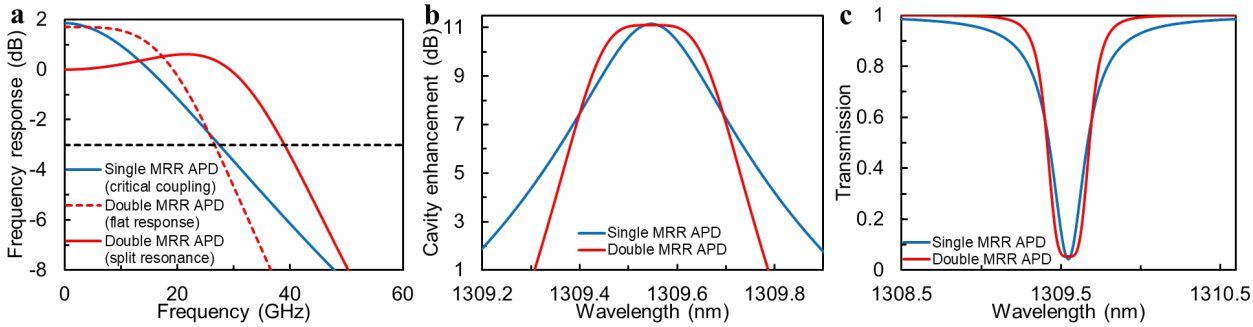

Supplementary Fig. 2 (a) Simulated frequency response, (c) simulated cavity enhancement, (c) simulated spectrum and crosstalk of single-MRR APD and double-MRR APD with flat "box-shape" response.

As the tradeoff simulation shown in Fig.2 (a), the double-MRR APD can achieve high responsivity when the coupling coefficient k_2 is low and it demonstrates a flat "box-shape" response spectrum. However, this design does not show significant improvement and achieves a similar bandwidth as the single-MRR APD. It demonstrates slight improvement at low frequency and shape roll-off at high frequency. The double-MRR APD with flat response has the similar cavity enhancement region as the single-MRR APD. Based on the frequency response comparison shown in Supplementary Fig. 2a, we chose to create a spectrum with a split resonance feature rather than a flat feature for a high bandwidth.

Optical spectrum simulation

To compare the experimental data with the theoretical model, the exact parameters value of the double-MRR configuration need to be obtained. Since the double-MRR structure has more parameters than the single-MRR structure, it is hard to directly fit and obtain parameters from spectrum. On the same wafer, we have the single-MRR structure with the same implantation condition and dimension. As shown in Supplementary Fig. 3a, the spectrum of single-MRR structure with 7.5 μm radius exhibits a DC extinction ratio of 17 dB and a full width at half-maximum (FWHM), Δλ, of ~0.24 nm. The red line is the Lorenzo-shape fitting to the measured spectrum. According to this, the round-trip field attenuation is ~0.966 and corresponding loss (α_{tot}) is 64 dB/cm. With the loss value, in Lumerical Interconnect, the spectrum of 8-channels double-MRR RX can be fitted as Supplementary Fig. 3b with channel spacing of 1.05 nm and FSR of 9.02 nm, which is close to the measured spectrum. The extracted k_1^2 is 0.18, k_2^2 is 0.02 and loss of first MRR is 3 dB/cm. The coupling coefficient is slightly higher than our designed value due to the fabrication error. The fitted spectrum also shows that channel crosstalk is negligible, and it can enable >8-channels operation. It should be noted than the spectrum can also be calculated using $\frac{|a_2^0(\Delta\omega)|^2}{T_{rt}}$ by varying the $\Delta\omega$ from Supplementary Eq. (11). The calculated spectrum is similar to the simulated spectrum in Lumerical.

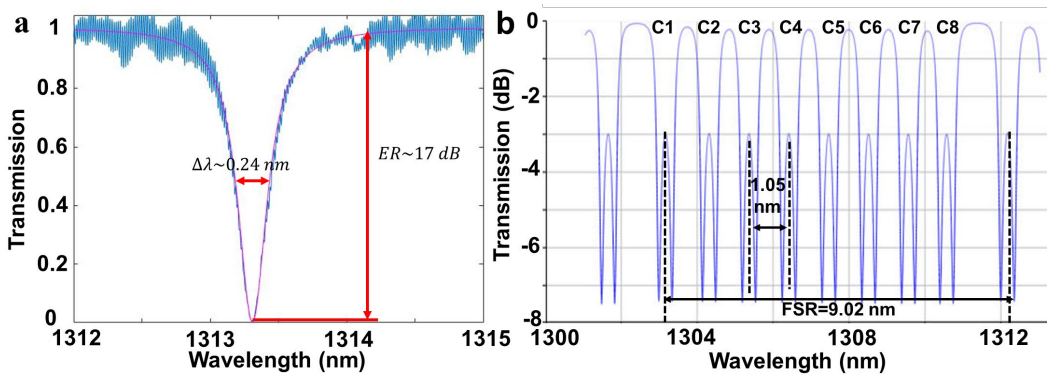

Supplementary Fig. 3. (a) Measured and fitted spectrum for single-MRR APD and (d) simulated spectrum of 8-channels double-MRR RX.

MRR APD Absorption Model

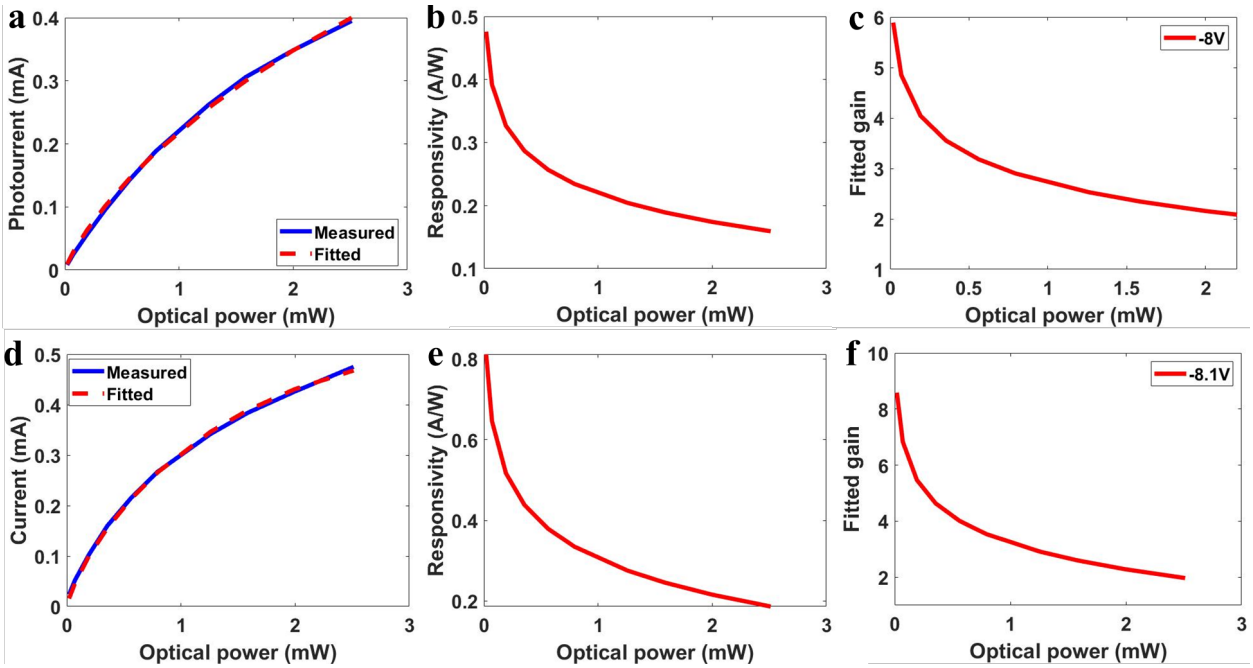

Supplementary Fig. 4. (a) Measured and fitted photocurrent, (b) fitted responsivity and (c) fitted avalanche gain versus bus WG power at -8V. (d) Measured and fitted photocurrent, (e) fitted responsivity and (f) fitted avalanche gain versus bus WG power at -8.1V.

For a MRR APD, as the increase of the bias voltage and electric field, both the PAT probability and avalanche gain will increase. Moreover, the resonant optical enhancement in an MRR structure can also enhance the absorption mechanism. A model, including all the contributing mechanisms for high responsivity in pure Si MRR photodetectors, is derived. We have identified three main mechanisms to include in this model: PAT, MRR resonance enhancement effect and avalanche gain. The two-photon absorption depending on the optical power intensity is weak and negligible for the low optical level. All symbols in the model are listed in Supplementary Table 1.

The photocurrent of the MRR APD can be expressed as [13]:

$$I_{photo} = P_i \cdot RE \cdot M \cdot \eta \frac{q}{hv} \tag{16}$$

where P_i is input optical power; RE is resonance enhancement; M is avalanche gain; η is internal quantum efficiency per round; q is charge and hv is photon energy. The resonance enhancement of the MRR structure is determined by the loss and coupling coefficients, which is extracted from spectrum.

The higher optical powers result in gain saturation, and the avalanche gain response commonly linearly decreases with optical power at a dBm scale. Consequently, the gain can be modeled as:

$$M = -a \cdot 10log_{10}(RE \cdot P_i) + b \tag{17}$$

where a and b are gain saturation fitting parameters.

The total light attenuation coefficient per roundtrip $\alpha_{tot} = \alpha_p + \alpha_l$ can be divided into two parts: α_p is the absorption coefficient to generate photocurrent which due to PAT and α_l is the loss coefficient which mainly comes from free carrier absorption. The internal quantum efficiency can be written as:

$$\eta = \frac{\alpha_p}{\alpha_{tot}}\left[1 - e^{(-\alpha_{total} \cdot L)}\right] = k \cdot \delta_r \tag{18}$$

where k is absorption ratio, L is MRR circumference and δ_r is the MRR propagation loss coefficient. The α_{tot} and corresponding δ_r are from the spectrum.

Based on the MRR APD absorption model, the photocurrent and responsivity versus optical power under different bias voltages can be plotted and fitted in Supplementary Fig. 4. At -8 V and -8.1V, the photocurrent shows a saturation trend with the increased optical power, and thus responsivity decreases from ~0.47 A/W to ~0.16 A/W and ~0.8 A/W to ~0.19 A/W, respectively. The parameters used in the model are listed in the Supplementary Table. 1. RE is simulated in Lumerical based on the known loss and coupling value. With the listed value, the calculated photocurrent achieves excellent agreement with the measured data. The fitted avalanche gain at -8 V at -8.1 V can reach to 5.9 and 8.9, respectively. Overall, the PAT contributes ~1.2 % absorption per roundtrip inside the MRR. The resonance enhancement (~7.1) and avalanche gain (~8.9) boost the absorption to enable a high total responsivity up to ~0.8 A/W at -8.1V.

Supplementary Table 1 | Symbol Meanings, Values, and Units for the MRR APD Absorption Model

Symbol	Meaning	Value	Unit
RE	Resonance enhancement	7.1	/
δ_r	Ring propagation loss coefficient	~0.0673	/
α_{tot}	attenuation coefficient	64	dB/cm
a	Gain fitting parameters	0.186(-8V), 0.32(-8.1V)	/
b	Gain fitting parameters	4.34(-8V), 6(-8.1V)	/
k	absorption ratio	18%	/
L	Effective PN junction length	47.2	μm

Noise measurement and analysis

The experimental setup for measuring the device noise is shown in Supplementary Fig. 5. In this setup, the DUT is probed with a ground-signal probe. The output signal was collected by a spectrum analyzer after amplifying by a TIA and a bias-tee.

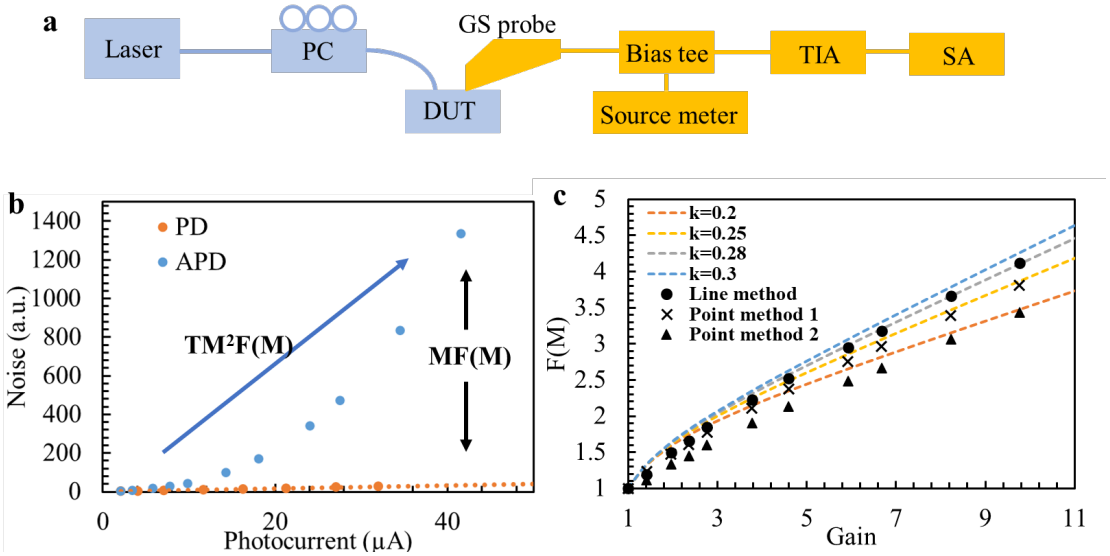

Supplementary Fig. 5. (a) Spectrum-analyzer-based noise figure measurement setup. (b) Measured noise under a fixed illumination intensity with increasing bias (APD curve), the measured noise under a fixed bias (-4 V) and varying illumination intensity (PD curve) and (c) excess noise factor using the point method and line method.

The noise produced by avalanche multiplication and PAT can be expressed as:

$$I_{shot}^2 = 2qM^2(TI_{photo} + I_{dark})F(M)\Delta f \tag{19}$$

where q is the electron charge; M is the multiplication gain; T is the PAT gain defined as the tunneling current at measured voltage divided by the tunneling current at unit gain point; $F(M)$ is the excess noise factor; Δf is the operating bandwidth; I_{photo} and I_{dark} are the photocurrent and dark current at unit gain, respectively. It should be noted that PAT will not happen without light and dark current-induced noise will not increase with the PAT.

Normally, the method to determine the APD's excess noise is to use a constant light intensity and change the bias to obtain different gain levels [14]. The noise without illumination is measured at each bias level and subtracted from the noise with illumination. The measurement results are shown as blue curve in Supplementary Fig. 5b. The excess noise factors of an APD were calculated by McIntyre model [15]:

$$F(M) = kM + (1-k)\left(2 - \frac{1}{M}\right) \tag{20}$$

where k is the ratio of the electron (α) and hole (β) impact ionization coefficients. For a MRR APD, when the bias voltage is at a sufficiently low bias such that there is no avalanche gain, that point can be used as a reference. Shot noise of the first point with avalanche gain (M=1) and PAT gain (T=1) can be expressed as:

$$I_{shot-photo-pointref}^2 = 2qI_{photo}F(M)\Delta f \tag{21}$$

By increasing the bias voltage, avalanche and PAT gain will increase. F(M) can be calculated as following:

$$F(M) = \frac{I_{shot-photo}^2}{M^2 T I_{shot-photo-pointref}^2} \tag{22}$$

where $I_{shot-photo}^2$ is measured noise under different higher bias with gain. This method works if the error of the first point measurement is small. The accuracy of the first point in a bias measurement is crucial, as it determines the quality of the subsequent points along the line. Any noise or uncertainty in the first point will propagate to the other points and affect the results. As the Supplementary Fig. 5c shows, the two black curves using point methods, where the first point were measured at two separate days. The change of $F(M)$ is visible and it represent the effect on the measured excess noise from the setup uncertainty noise.

One approach to address this issue is to use a reference line so that the measured points are independent of each other [16]. The MRR APD is biased at a low voltage (-4 V) to ensure unity gain. The noise is measured at the fixed bias by changing the intensity of the incident light as shown by the orange points in Supplementary Fig. 5b, which only represents the noise from the photocurrent. The points are fitted with a straight line and the fitted curve are used to calculate the $F(M)$ as follows:

$$F(M) = \frac{I_{shot-photo}^2}{M I_{shot-photo-lineref}^2} \tag{23}$$

$I_{shot-photo-lineref}^2$ is the fitted PD noise at the same photocurrent as the corresponding blue point. Note that only M is being divided instead of M^2T since reference line already accounts for factor of MT via the

increase in photocurrent. During the calculation, the MT can be obtained based on the photocurrent at higher bias divided by the photocurrent at unit gain. The M is fitted using the method in last section. For the calculated $F(M)$ using this method, as the noise of the first point changes, none of the subsequent points are affected. Therefore, this line reference method offers a more robust noise calculation.

S-parameter measurement

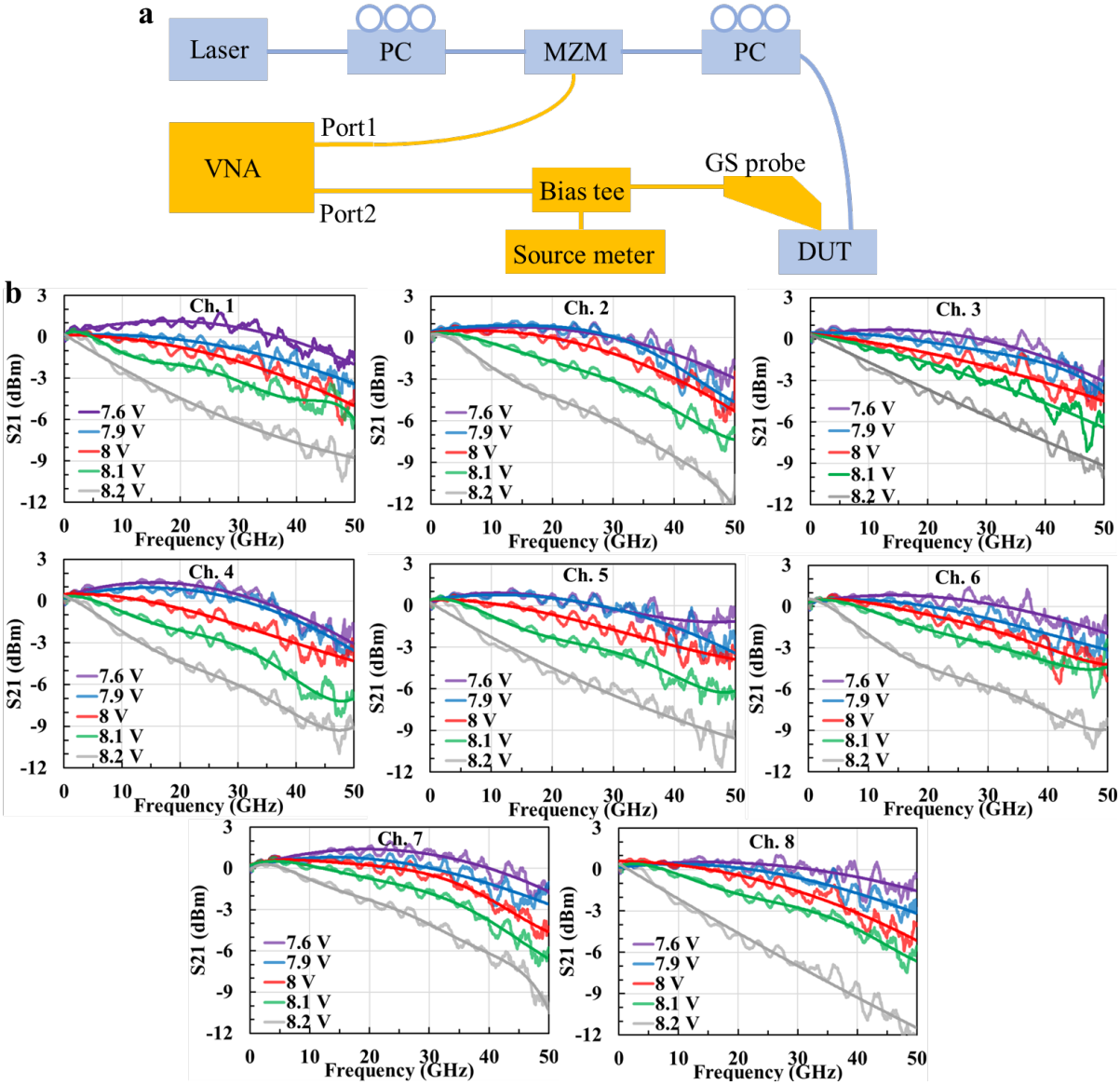

Supplementary Fig. 6. (a) Bandwidth measurement setup and (b) measured S21 frequency response at different bias voltage for all 8-channels

The experimental setup for measuring the device bandwidth is shown in Supplementary Fig. 6. A 1310 nm laser emitted a continuous wave (CW) optical signal, which was polarized by a controller and then modulated by a lithium niobate (LiNbO3) Mach-Zehnder modulator (MZM). The MZM was biased at the quadrature point and driven by a vector network analyzer (VNA). The modulated optical signal was injected into the double-MRR RX using a grating coupler and the photoresponse was extracted using a ground-

signal probe. The radio frequency photoresponse was measured by the VNA with a bias-tee. Circuit and line losses were calibrated out for the measurement.

At each bias voltage, the |S21| response was measured at the resonance wavelength. Each channel device was measured at -7.6 V, -7.9 V, -8 V, -8.1 V, and -8.2 V, respectively. The |S21| results also show good uniformity. At -7.6 V, the double-MRR APD shows 3-dB bandwidth of >50 GHz, which agrees with our simulation results and is mainly limited by the photon lifetime. The bandwidth declines to ~40 GHz at -8 V at a responsivity of ~0.4 A/W, ~35 GHz at -8.1 V with a responsivity of ~0.8 A/W and ~15 GHz at -8.2 V at a responsivity of ~3 A/W. With the increase of the voltage, gain will increase rapidly, and the avalanche build-up time dominates the bandwidth limitation. We observe a trade-off between bandwidth and responsivity. The gain-bandwidth product GBP are ~236 GHz and ~311 GHz at a bias voltage of −8 V and -8.1 V at −16.5 dBm input. The GBP is comparable to the conventional Si–Ge and III–V APDs.

Eye diagrams and bit error rate measurement

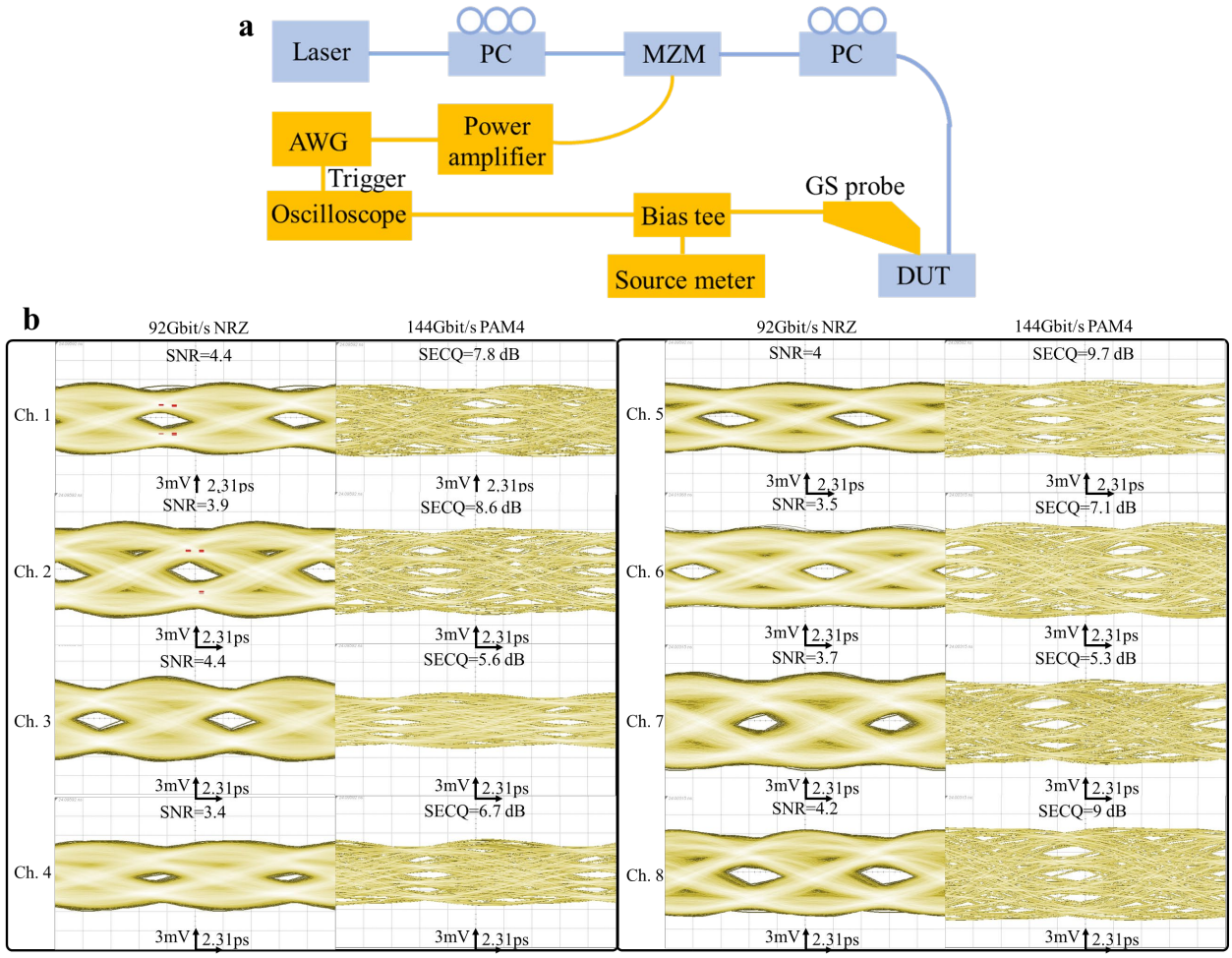

Supplementary Fig. 7 (a) Eye diagrams measurement setup and (b) Measured 92 Gb/s NRZ and 144 Gb/s PAM-4 eye diagrams without equalization.

A commercial tunable CW laser, Santec TSL 570, was used as the input optical source with output of 18 dBm. The modulated signal was applied by an AWG and amplified by a power amplifier. After MZM modulator, signal was detected by a double-MRR APD without a TIA, which produced eye diagrams that

were recorded using a DCA. The Thorlab MX65E-1310 modulator, polarization controller and grating coupler results in a total loss of ~ 15.5 dB. Therefore, the optical power reaching the chip is less than 2.5 dBm. To enhance the eye diagram quality, we need to reduce the optical losses and increase the power at the chip level.

The eye diagrams of the 8-channel RX were measured with pseudo-random bit sequence 7 (PRBS7) patterns at the bias of -8 V as shown in Supplementary Fig. 7. All raw eye diagrams are measured without any FFE and the eye diagrams improved with FFE are shown in Fig. 5. The left column is the eye diagrams at 92 Gb/s NRZ without averaging. All eyes are open and symmetrical, which exhibit a signal-to-noise ratio of 3.4 to 4.4. The circuit noise from oscilloscope lead to relatively high noise at both "0" and "1" levels.

PAM4 is an efficient way to obtain higher bit rates with limited bandwidth. In this work, we measured the 72 Gbaud (144 Gb/s) PAM4 eye diagrams without FFE for all 8-channels and the SECQ was also measured at SD-FEC threshold of symbol error rate< 4.8E-4 (IEEE 802.3cd). The PAM4 diagrams were measured with 8 times averaging to suppress the circuit noise. The SECQs penalty of the 72 Gbaud eye diagrams is from 5.6 dBm to 9.7 dBm. The eye diagrams can be further improved with a higher bandwidth AWG and a lower noise oscilloscope.

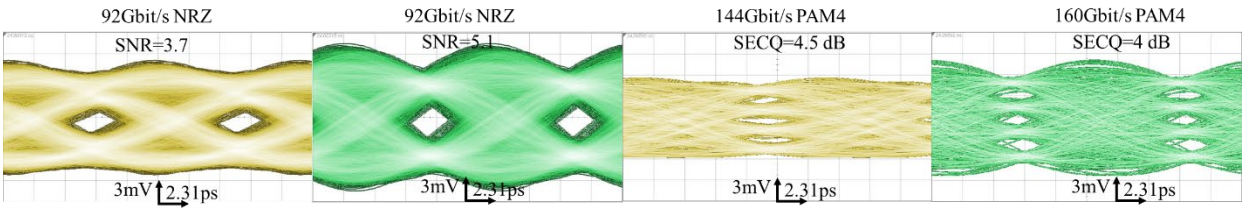

Supplementary Fig. 8. Measured 92 Gb/s NRZ w/o FFE, 144 Gb/s PAM4 without FFE and 160 Gb/s PAM4 eye diagrams with FFE using PRBS9.

As the Supplementary Fig. 8 shows, the eye diagrams of the double-MRR APD were also measured with pseudo-random bit sequence 9 patterns at the bias of -8 V. The yellow figures are measured without FFE, and green figures are measured with 8-tap feed forward equalization. The signals are significantly improved with the FFE. The measured SNR for NRZ signal and SECQ for PAM4 signals does not degrade a lot from PRBS7 to PRBS9.

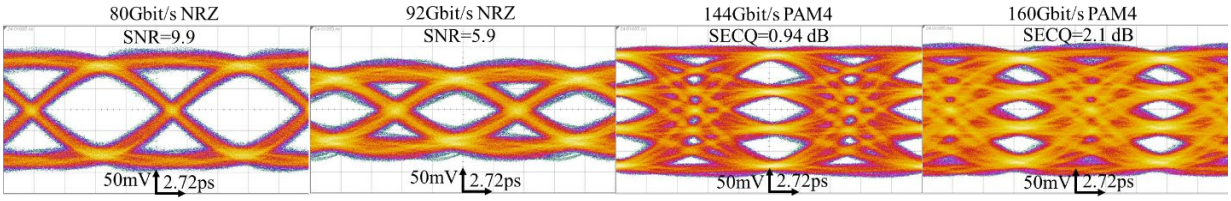

Supplementary Fig. 9. Measured 80 Gb/s NRZ, 92 Gb/s NRZ, 144 Gb/s PAM4 and 160 Gb/s PAM4 eye diagrams with AWG directly connected to oscilloscope.

According to the M8194A data sheet, the 120 GSa/s arbitrary waveform generator (AWG) can generate frequency content up to 50 GHz. Supplementary Fig. 9 shows the eye diagrams for setup AWG directly connected to oscilloscope. The signal quality drops quickly as the data rate gets higher. For NRZ signals, the SNR goes down from 9.9 to 5.9 when the data rate changes from 80 Gb/s to 92 Gb/s. For PAM4 signals, the SECQ gets worse from 0.94 dB to 2.1 dB when the data rate changes from 144 Gb/s to 160 Gb/s. 92 Gb/s NRZ and 160 Gb/s PAM4 signals are the upper limit of the experimental setup. Our measurement reached this capacity and tested the limits of the setup. The highest swing voltage Vpp of the AWG is 0.8

V, therefore 60 GHz electrical power amplifiers were added to amplify the swing voltage. The combination of modulator, electrical power amplifiers, bias-tees, probes, and RF cables results in a loss of ~9.5 dB at 40 GHz and ~ 12 dB at 50 GHz. The signal distortion caused by these components was calibrated by the AWG internal calibration tool, while resulting in reducing the Vpp of the AWG and signal quality. A higher data rate is achievable with higher bandwidth AWG and RF components.

For the measurement setup, the total noise of levels "1" and "0" mainly consisted of three parts: APD shot noise, laser RIN noise, and electric circuit noise, which includes thermal noise and oscilloscope amplifier noise. The noise can be expressed as:

$$I_{total}^2 = I_{shot}^2 + I_{RIN}^2 + I_{circuit}^2 \tag{24}$$

where I_{shot}^2 is expressed in Eq. (2); $I_{RIN}^2 = I_{photocurrent}^2 \cdot RIN \cdot M^2 \cdot BW$; $I_{circuit}^2$ can be assumed to be a constant. The RIN noise is measured to be -150 dB/Hz for this setup, and it is relatively small in the system. The $I_{circuit}^2$ can be measured on the oscilloscope without any light in. $I_{circuit}^2$ dominates the whole noise when the optical power is weak. To get rid of the effect of large circuit noise for the accurate APD measurement, the $I_{circuit}^2$ is subtracted from the measured I_{total}^2 to obtain a bit-error-rate after calibration. The actual sensitivity after calibration can be improved by more than 1 dB for 92 Gbit/s signal as shown in Fig. 5c. As discussed, the $I_{circuit}^2$ plays important role for the measurement. All the eye diagrams in the paper are raw eye diagrams and the performance can be improved with an off-chip DSP to remove the additional circuit noise.

Double MRR APD Absorption Mechanism

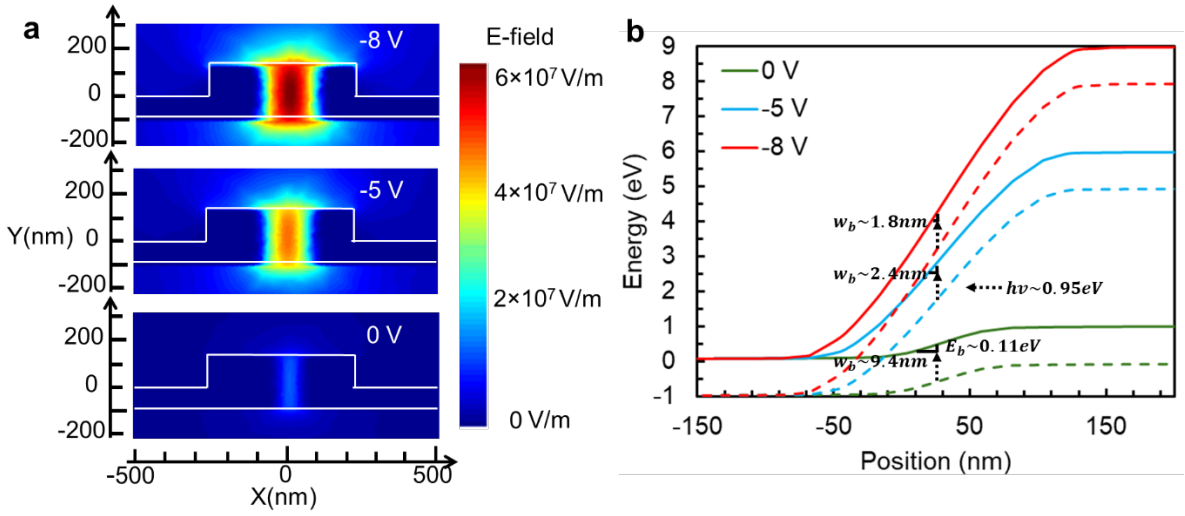

Supplementary Fig. 10. Simulated (a) electric field and (b) energy band diagrams of the Si PN junction at different bias voltages.

To qualitatively understand the light absorption phenomena, we simulated electric field distributions and the band structure of the silicon PN junction at 0, −5, and −8V as shown in Supplementary Fig. 10. With increased bias, a strong electric field across the junction shorten the effective tunneling width w_b. The reduction of w_b for this triangular barrier results in the exponential increase of tunneling probability, which can be written as [13, 17]:

$$T \approx exp\left(-\frac{4\sqrt{2m^*}}{3\hbar}\sqrt{E_b}w_b\right). \tag{25}$$

where m^* is the effective mass of electrons of Si; w_b is the effective barrier width; b is the PAT coefficient; E_b is the potential barrier height, which corresponds to the $E_g - h\nu \approx 0.11\ eV$ at 1310 nm. It should be noted the bandgap will narrow with the existence of the dopants. As shown in simulation, w_b decreases from ~ 9.4 nm at 0 V to ~ 2.4 nm at -5 V to ~ 1.8 nm at -8 V. This makes it easier for the valence band electrons to cross the energy gap and enter the conduction band through a process known as photon-assisted tunneling. Tunneling probability at -8 V increases exponential by a factor of 3.3 × 105 and 2.7 compared to tunneling probability at 0 V and -5 V, respectively. By increasing reverse bias, the electric field inside the junction becomes stronger and depletion region becomes wider. It greatly increases not only the tunneling probability but also the overlap of optical mode with depletion region. Therefore, the sub-bandgap absorption effect will be much more significant at high reverse-bias voltage. In addition, as shown in Supplementary Fig. 10 (a), the maximum electric field of the Si PN junction at −8 V is > 6 × 107 V/m. Such a high electric field is sufficient to trigger impact ionization in silicon. Accordingly, avalanche gain would also contribute to the overall responsivity at high reverse-bias voltage.

Double MRR APD Saturation Characteristic

The receiver's saturation power is a key parameter that indicates the highest input power level that the receiver can process without introducing distortion. However, due to the gain saturation, APDs exhibit a strong nonlinearity in the RF output power. The space charge effect is a major cause of this phenomenon. The intrinsic region absorbs light and creates electron and hole pairs. These pairs are amplified by the avalanche effect and move toward the anode and cathode. Due to the limitation of carrier velocity, the excess charges accumulate near the edges of the depletion region and create an electric field that opposes bias. This electric field is distorted by these charges and causes a stronger space charge effect that reduces the impact ionization process as the optical power increases. Although it is hard to define saturation power for APD, the analysis of the output power versus input powers for our device is still important and helpful.

The photocurrent of the microring APD were measured and plotted as a function of the input optical power in Supplementary Fig. 11 (a). We can observe strong gain saturation due to the space charge effect as the optical power increases. The RF output power of APD exceeds the theoretical power that would be obtained from a PD with the same responsivity at unit gain, as shown in Supplementary Fig. 11 (b). This is attributed to the avalanche gain of the MRR APD. It should be noted that the RF output of our experiment is constrained by the components of our test setup. The electrical power amplifiers, bias-tees, modulator, and RF cables have 3dB bandwidths of 60 GHz, 50 GHz, 65 GHz, and 50 GHz, respectively. This leads to a loss of ~ 9.5 dB at 40 GHz. We show the calculated results with and without considering the setup loss as APD with loss and APD without loss, respectively. As shown in Supplementary Fig. 11 (c), the RF compression is calculated to decrease rapidly as the photocurrent increases due to gain saturation.

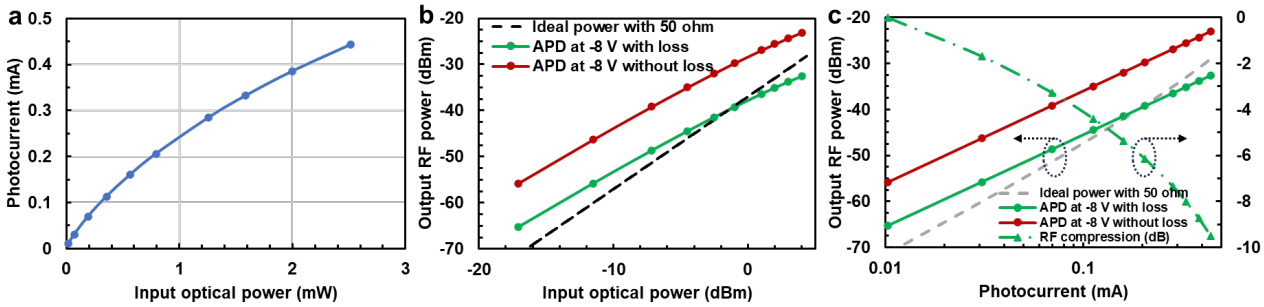

Supplementary Fig. 11. (a) Photocurrent versus input optical power, (b) RF output power of MRR APD versus input output power and (c) RF output power and compression versus average photocurrent.

APD experiences the strong nonlinearity with increased optical power, but this is not a problem for APD applications. APD are mainly used to detect relatively weak signals. For telecommunication applications, the typical input power range for APDs is from -20 dBm to -10 dBm. We conducted most of our experiments at -16 dBm, which is consistent with the actual operating condition.

Double MRR APD Discussion

As the model developed in Supplementary MRR APD Absorption Model section, photon-assisted tunneling converts ∼1.2 % light to photocurrent per round-trip inside the cavity, and the MRR enhancement effect (∼7.1×) boost responsivity to 0.086 A/W with avalanche gain. There are three ways to further improve responsivity. The first approach is to adopt "Z" shape doping profile as shown in Supplementary Double-MRR RX with "Z" shape doping profile section. The junction is created with two heavy P and N doping concentration and two light P and N doping concentration. As Supplementary Fig. 1(a) shows, the junction interface enables a better mode to overlap by ~35% between the high electric field and the optical mode and improves the absorption probability. We prove the feasibility of the all-silicon double-MRR RX in a standard Si photonics process at AMF. The measured results agree with simulated results verify that the novel structure improves the responsivity by ~35% with the same high-speed performance as Supplementary Fig. 1(d) and (e) shows. The responsivity of our MRR PD is improved to ~0.12 A/W.

It should be noted the current implantation condition is optimized for modulators, not for the APD, which results in a high doping level that causes more free carrier absorption loss and reduces the MRR enhancement effect. The second solution is to decrease the doping concentration. We demonstrate the all-silicon MRR APD with lower doping concentration at Leti, which can achieve a responsivity of >65 A/W [17]. For a conservative estimation, the MRR enhancement effect can be doubled without compromising the bandwidth. The responsivity of our MRR PD can be increased to ~0.24 A/W.

In addition, the all-silicon PD can achieve higher responsivity by creating lattice defects with related deep-level charge states [23-26]. A deep level with a charge-state energy below the conduction band can produce photocurrent by optically exciting an electron from the valence band to the deep level state, and then thermally transferring the carrier to the conduction band. We can use Si+ ion implantation to create lattice defects in a controlled way, which is also compatible with Silicon photonics process. We can make devices with both photo-assisted tunneling and defect-mediated absorption with an extra doping layer based on our process. As ref [23] shows, 4.5 % light can be absorbed for 50 μm length waveguides by defect-mediated absorption. The enhanced MRR enhancement effect can boost overall responsivity to ~0.87 A/W, which is comparable to the conventional PD.

We model the frequency response of the MRR PD with and without gain, and show that the bandwidth can reach larger than ~60 GHz at low gain region as shown in Supplementary Fig. 12 (a). For more simulation details, please refer to the Supplementary Analytic Model section. To obtain the frequency response over 50 GHz, we also measured the bandwidth of the double MRR APD with "Z" shape doping profile using another VNA up to 65 GHz. At this region, APD can achieve more than 55 GHz operation as shown in Supplementary Fig. 12 (b). At the low gain region of -7.5 V, the APD shows a 3 dB bandwidth of ~ 55 GHz. One possible source of discrepancy between the experimental and simulated results is the absence of a suitable calibration kit that can operate at frequencies up to 50 GHz. This may lead to an underestimation of the bandwidth in the measurements. The internal bandwidth–efficiency product of our device is 50 GHz. Based on the bandwidth, the device can support at least 200 Gb/s per channel, maybe up to 240 Gb/s per channel.

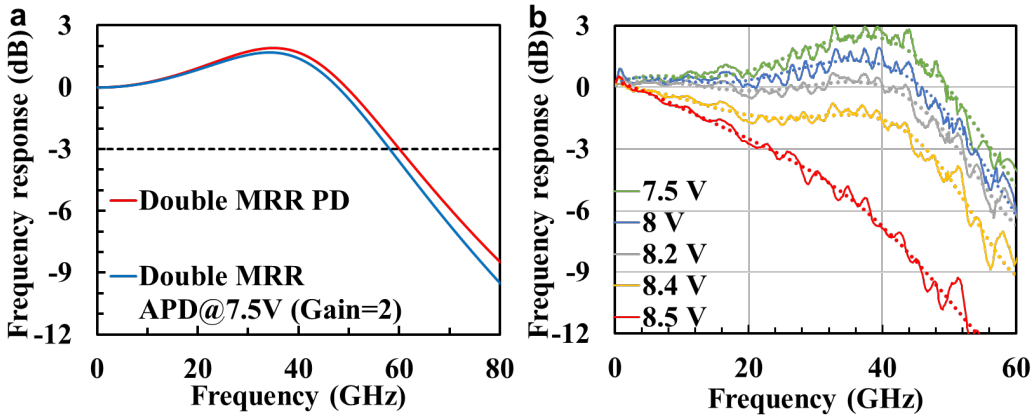

Supplementary Fig. 12. (a) simulated and (b) measured frequency response for double MRR APD with "Z" shape doping profile

Compared to conventional APD, our MRRs can also function as demultiplexer. Thanks to the suppressed channel crosstalk as shown in Fig. 3, if the 5-μm radius MRR was adopted, our double MRR APDs can enable an 18-channels DWDM link within a single FSR with less than less than -40 dB crosstalk. Assuming a conservative estimation, a single chip can achieve 18×200 Gb/s (3.6 Tb/s). The single mode spectral efficiency can reach up to 1.53 bit/s/Hz for a single device, that would be much higher than the commercial receiver.

Regarding the state-of-the-art Si-Ge PD in Ref. [27], the results are quite impressive. It shows internal responsivities of 0.3 A/W (265 GHz) and 0.45 A/W (240 GHz). The internal bandwidth–efficiency product of the device is 86 GHz. However, for their ingenious germanium-fin design, the narrowest fin width is only ~ 60 nm, which limits the compatibility of their device with existing Si photonics fabrication platforms. For instance, Leti and AMF have a minimum feature size of 140 nm. Features smaller than that are not reliable and gaps below 100 nm cannot be created. Moreover, the germanium-FinFET structure is not standard in the foundry. The process is specific for this PD fabrication. The small feature requirements and process change may lead to reliability and yield issue. Our approach provides a distinctively simple and accessible route to realize PD in standard silicon foundry processes.

The next generation of optical interconnects with 1.6 Tb/s capacity, which requires 100 Gb/s or 200 Gb/s per line. Some of the leading research groups in this field are II-VI Inc. and Intel Inc., who have demonstrated their use of photodetectors with high responsivity and bandwidth for their optical interconnect prototypes. II-VI Inc. used a PD with 0.82 A/W responsivity and supporting 106 Gb/s eye diagrams [28], while Intel Inc. used a PD with 0.66 A/W responsivity, 50 GHz bandwidth and supporting 200 Gb/s [29]. In contrast, our double MRR resonator APD can achieve better performance than these most-recent PD used for the next generation of optical interconnects.

Wavelength Stabilization

The performance of MRR resonator is sensitive to fabrication variation and external conditions, such as temperature and humidity. This poses a challenge for its practical application. To address this, we need a circuit to automatically tune and stabilize the wavelength of the double MRR resonator to ensure its optimal performance.

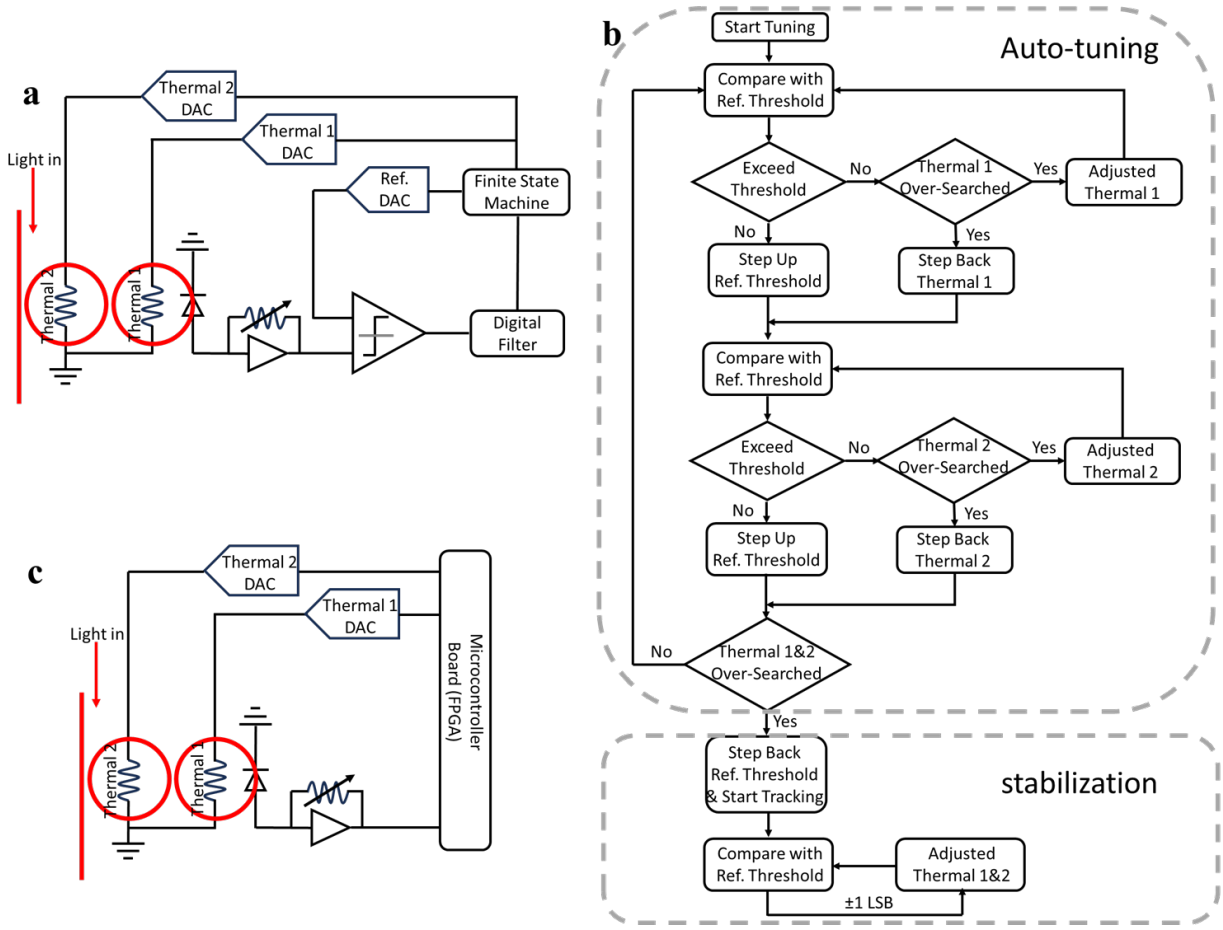

Supplementary Fig. 13 (a) Block diagram of CMOS circuit-based wavelength stabilization circuit; (b) flow-chart of wavelength stabilization process and (c) block diagram of FPGA based wavelength stabilization circuit.

To adjust and lock the wavelength, CMOS thermal control circuits with feedback loops are often used. CMOS thermal tuning schemes with integrated heating resistors are common in the current MRR resonator-based transceiver and switch system [30-32]. Typically, multi-ring systems are designed such that the resonance of all the MRRs are aligned with the input laser's wavelength. If split resonance is needed, the MRR response can be adjusted after the initial alignment. Our double MRR APD design has a unique feature: the photocurrent on the second MRR can directly monitor the degree of resonance aligning with the laser wavelength. This eliminates the need for external PDs to monitor the power levels at through and drop port. We can align the resonances of the two MRR by tuning them sequentially to maximize the photocurrents. The circuit for stabilizing the wavelength based on the photocurrent is shown in Supplementary Fig. 13(a). It consists of two current segmented digital-to-analog converters (DACs) for individual heaters control, a DAC for reference, a simple resistor based low-pass TIA, a filter and a Finite State Machine (FSM) controller. The photocurrent from the integrated photodetector is converted to voltage by the resistor TIA. The voltage is then compared with the reference DAC output by a sense amplifier. The FSM receives comparator output after digitally filter the for closed-loop control. The CMOS circuit logic has the following steps, as illustrated in Supplementary Fig. 13(b). The first phase is to align the wavelength automatically. To do this, the reference DAC is set to a safe reference level, which corresponds to a stable point on the resonator curve. This means that the voltage is neither too low nor too high, to avoid locking to noise or zero values in the resonator curve. We use thermal 1 and 2 to tune the temperature of MRR 1 and 2. However, we can observe non-negligible thermal crosstalk between the MRR at the same channel

as shown in Supplementary Fig. 14, which means that we cannot control the two thermal heaters independently. It should be noted there was no significant thermal crosstalk between the different channels, due to their large separation. As shown in flowchart, we keep comparing the signals with reference DAC and gradually tune MRR 1 and 2 one by one with two feedback loops. After each comparison is achieved, the reference DAC saves the successful locking point and then increases gradually in a trail-and-error fashion to search for the temporary maximized photocurrent. When one of the MRRs 1 or 2 reaches its maximum photocurrent temporarily, subsequent increasing of the reference level will trigger an over-searching signal. This is detected and the reference DAC is stepped back with an offset to the last successful locking point and then allows the other MRR to adjust for a higher photocurrent. When both of the MRR trigger the over-searching signals, it means maximum photocurrent has been achieved and auto-alignment process is finished. The second phase is background wavelength stabilization. In this phase, the FSM reuses the digital filter to realize bang-bang type feedback. Based on the output of digital filter, the thermal DAC adjusts one least significant bit up or down for small shift at one cycle to compensate for temperature changes caused by the environmental factors such as thermal or humidity change. Our APDs have low optical channel crosstalk, which allows us to adjust one channel at a time by measuring the respective photocurrent. This way, we can avoid interference between the channels.

A simple way to tune the wavelength for small-scale experiments is to use microcontroller boards like FPGA, as shown in the schematic diagram Supplementary Fig. 13(c). The coordinate descent algorithm [33, 34] can be applied by changing the voltage in small steps and measuring the photocurrent, and then selecting the tuning that gives the highest reading. The algorithm cycles through the coordinate directions (thermal 1 and 2), reducing the problem to two one dimensional optimization subproblems along each coordinate direction (i.e., a line-search), using the optimum value in the current direction as the starting point for the search in the next direction. Coordinate descent algorithm usually refers to minimization, but we use it for maximization by minimizing the negative of the objective function. Any detuning that occurred in the MRRs due to thermal crosstalk can be accounted for in optimization process. This algorithm is available as SciPy.Optimize in Python library.

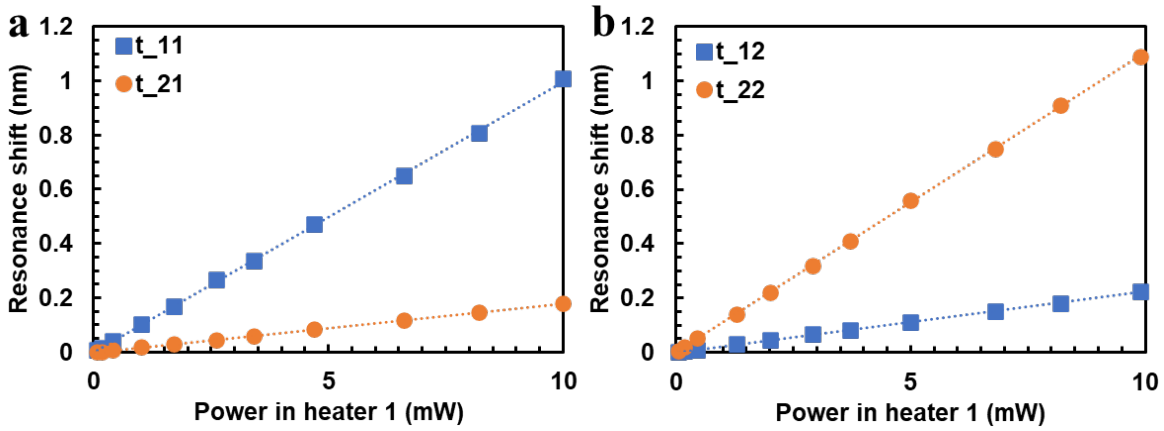

Supplementary Fig. 14. Resonant wavelength shifts due to same-ring heating and thermal crosstalk for (a) heater 1 and (b) heater 2.

Another continuous tuning of a double silicon MRR is using a calibration look-up table [35, 36]. By recording the MRR resonance wavelengths under different power, strongly correlated linear tuning curves can be obtained in the presence of thermal crosstalk effects on the resonant frequencies as shown in Supplementary Fig. 14. The resonance shift of each individual MRR was determined by measuring the resonance wavelength of that MRR at the output port when it was sufficiently detuned from the other. From the linear best fit lines of the shifts due to same-ring heating, we obtain same-ring thermal tuning rates of t_{11} = 99.6 pm/mW for MRR 1 and t_{22}= 110.6 pm/mW for MRR 2. We also note that each MRR in the same channel experienced significant thermal crosstalk. The rate of resonance changes of MRR 1 due to

heater 2 is t_{12} = 22.4 pm/mW and that of MRR 2 due to heater 1 is t_{21} = 18 pm/mW. The general relation between the frequency shift of each MRR and the electrical power delivered to the respective heater can be represented by the response matrix:

$$\begin{bmatrix}\Delta\lambda_1\\ \Delta\lambda_2\end{bmatrix} = \begin{bmatrix}t_{11} & t_{12}\\ t_{21} & t_{22}\end{bmatrix}\begin{bmatrix}P_1\\ P_2\end{bmatrix} \tag{26}$$

where the tuning rates t_{11}, t_{12}, t_{21}, and t_{22} are given above. The tuning matrix allows the double MRR to be tuned to any arbitrary wavelength without the need for further optimization. As for background wavelength stabilization stage due to environment fluctuations, for example, the change in resonant wavelength as a function of waveguide temperature variation can be expressed as [37]:

$$\Delta\lambda_r(\Delta T) = \lambda_r[1 + \left(\in + \frac{1}{n_g}\frac{dn}{dT}\right)\Delta T] \tag{27}$$

where $\in$ and n_g are the thermal expansion coefficient and group index of the MRR. dn/dT is the index thermo-optic coefficient of silicon, which is ~1.94×10-4 K-1 at 1310 nm. Since the resonance changes almost in linearity with the temperature, the required the tuning power under different temperature variation can be obtained with equation (26) and (27) if we know the temperature variation from thermometer. Other environment variation can be calibrated using the same method.

For our measurements, we need to adjust the thermal wavelength shift by about 500 pm at most and 250 pm on average to account for the fabrication variation. The required thermal tuning power per MRR is 2.4 mW. The thermal control of the circuit consists of 4 op-amps for feedback control [38, 39], plus 2 op-amps for TIA and comparator, making a total of 6 op-amps. These op-amps have a bandwidth of about ~MHz and can be implemented in CMOS technology with a power consumption of only 20 μW each. Moreover, DAC can also be realized in CMOS technology, with a power consumption of 100 μW [40]. Therefore, the total power consumption of the thermal control is estimated to be 5.2 mW per channel. Assuming a data signal of 160 Gb/s for the MRR resonator, the power consumption of the thermal control is equivalent to 32.6 fJ/bit. To minimize the effects of thermal crosstalk, which complicates the tuning process, some thermal isolation methods can be implemented. For example, air trenches can be etched near and below the MRR waveguides to reduce heat transfer. In addition, this can increase the thermal tunning efficiency to about 300 pm/mW [41, 42]. As a result, the power consumption of the thermal control can be reduced to 2 mW per channel and 12.6 fJ/bit.

References

1. Yuan, Yuan, et al. "High responsivity Si-Ge waveguide avalanche photodiodes enhanced by loop reflector." IEEE Journal of Selected Topics in Quantum Electronics 28.2: Optical Detectors (2021): 1-8.

2. X. Wu, D. Huang, T. Kim, R. Kumar, G. Su, C. Ma, S. Liu, G. Balamurugan, and H. Rong, "Fully integrated dual-polarization silicon photonic transceiver with automated polarization control," in Optical Fiber Communication Conference (OFC) 2023, Technical Digest Series (Optica Publishing Group, 2023), paper Tu2E.3.

3. Peng, Yiwei, et al." High-Speed All-Silicon Double Microring Avalanche Photodetectors." OECC, 2023

4. Chu, Sai Tak, et al. "Cascaded microring resonators for crosstalk reduction and spectrum cleanup in add-drop filters." IEEE Photonics Technology Letters 11.11 (1999): 1423-1425.

5. Little, Brent E., et al. "Microring resonator channel dropping filters." Journal of lightwave technology 15.6 (1997): 998-1005.

6. Little, B. E., et al. "Wavelength switching and routing using absorption and resonance." IEEE Photonics Technology Letters 10.6 (1998): 816-818.

7. Melloni, Andrea. "Synthesis of a parallel-coupled ring-resonator filter." Optics letters 26.12 (2001): 917-919.

8. Pile, Brian, and Geoff Taylor. "Small-signal analysis of microring resonator modulators." Optics Express 22.12 (2014): 14913-14928.

9. Yuan, Yuan, et al. "A 100 Gb/s PAM4 two-segment silicon microring resonator modulator using a standard foundry process." ACS Photonics 9.4 (2022): 1165-1171.

10. Peng, Yiwei, et al. "Analytical Modeling of Silicon Microring Photodetectors." 2022 IEEE Photonics Conference (IPC). IEEE, 2022.

11. Mai, Yu Xiang, and Gang Wang. "Equivalent circuit modeling of separate absorption grading charge multiplication avalanche photodiode." Journal of Lightwave Technology 27.9 (2009): 1197-1202.

12. Wu, Jiayin, and Gang Wang. "A novel equivalent circuit model for separate absorption grading charge multiplication avalanche photodiode (APD)-based optical receiver." Journal of Lightwave Technology 28.5 (2009): 784-790.

13. Yuan, Yuan, et al. "Mechanisms of enhanced sub-bandgap absorption in high-speed all-silicon avalanche photodiodes." Photonics Research 11.2 (2023): 337-346.

14. Yuan, Yuan, et al. "Temperature dependence of the ionization coefficients of InAlAs and AlGaAs digital alloys." Photonics Research 6.8 (2018): 794-799.

15 R. J. McIntyre, "Multiplication noise in uniform avalanche diodes," in IEEE Transactions on Electron Devices, vol. ED-13, no. 1, pp. 164-168, Jan. 1966, doi: 10.1109/T-ED.1966.15651.

16. Dadey, Adam A., et al. "Considerations for excess noise measurements of low-k-factor Sb-based avalanche photodiodes." JOSA A 40.6 (2023): 1225-1230.

17 Peng, Yiwei, et al. "All-silicon microring avalanche photodiodes with a> 65 A/W response." Optics Letters 48.5 (2023): 1315-1318.

18 Gao, Meijun, Chao Li, and Zhengyuan Xu. "Optimal transmission of VLC system in the presence of LED nonlinearity and APD module saturation." IEEE Photonics Journal 10.5 (2018): 1-14.

19 Parks, Joseph W., et al. "Theoretical study of device sensitivity and gain saturation of separate absorption, grading, charge, and multiplication InP/InGaAs avalanche photodiodes." IEEE transactions on electron devices 43.12 (1996): 2113-2121.

20 Wang, Binhao, and Jifang Mu. "High-speed Si-Ge avalanche photodiodes." PhotoniX 3.1 (2022): 1-22.

21 Xiang, Yuluan, et al. "High-speed waveguide Ge/Si avalanche photodiode with a gain-bandwidth product of 615 GHz." Optica 9.7 (2022): 762-769.

22 Virot, Léopold, et al. "Germanium avalanche receiver for low power interconnects." Nature communications 5.1 (2014): 4957.

23 Geis, M. W., et al. "Silicon waveguide infrared photodiodes with> 35 GHz bandwidth and phototransistors with 50 AW-1 response." Optics Express 17.7 (2009): 5193-5204.

24 Grote, Richard R., et al. "10 Gb/s Error-Free Operation of All-Silicon Ion-Implanted-Waveguide Photodiodes at 1.55$\mu {\rm m} $." IEEE Photonics Technology Letters 25.1 (2012): 67-70.

25 Li, Xianyao, et al. "40 Gb/s all-silicon photodetector based on microring resonators." IEEE Photonics Technology Letters 27.7 (2015): 729-732.

26 Casalino, Maurizio, et al. "State‐of‐the‐art all‐silicon sub‐bandgap photodetectors at telecom and datacom wavelengths." Laser & Photonics Reviews 10.6 (2016): 895-921.

27 Liao et al., "Silicon Photonics for Next-Generation Optical Connectivity," 2023 Optical Fiber Communications Conference and Exhibition (OFC), San Diego, CA, USA, 2023, pp. 1-3, doi: 10.1364/OFC.2023.Th3B.1.

28 J. Eng. "Optoelectronic Components for Communications and Sensing." Optical Fiber Communication Conference. Optica Publishing Group, 2023.

29 Lischke, S., et al. "Ultra-fast germanium photodiode with 3-dB bandwidth of 265 GHz." Nature Photonics 15.12 (2021): 925-931.

30 Li, Hao, et al. "A 25 Gb/s, 4.4 V-swing, AC-coupled ring modulator-based WDM transmitter with wavelength stabilization in 65 nm CMOS." IEEE Journal of Solid-State Circuits 50.12 (2015): 3145-3159.

31 Li, Cheng, et al. "Silicon photonic transceiver circuits with microring resonator bias-based wavelength stabilization in 65 nm CMOS." IEEE journal of solid-state circuits 49.6 (2014): 1419-1436.

32 Sharma, Jahnavi, et al. "Silicon photonic microring-based 4× 112 Gb/s WDM transmitter with photocurrent-based thermal control in 28-nm CMOS." IEEE Journal of Solid-State Circuits 57.4 (2021): 1187-1198.

33 Mak, Jason CC, et al. "Automatic resonance alignment of high-order microring filters." IEEE Journal of Quantum Electronics 51.11 (2015): 1-11.

34 Jayatilleka, Hasitha, et al. "Automatic configuration and wavelength locking of coupled silicon ring resonators." Journal of Lightwave Technology 36.2 (2017): 210-218.

35 Dahlem, Marcus S., et al. "Reconfigurable multi-channel second-order silicon microring-resonator filterbanks for on-chip WDM systems." Optics Express 19.1 (2011): 306-316.

36 Ren, Yang, et al. "A continuously tunable silicon double-microring filter with precise temperature tracking." IEEE Photonics Journal 10.6 (2018): 1-10.

37 Xu, D.X.; Delâge, A.; Verly, P.; Janz, S.; Wang, S.; Vachon, M.; Ma, P.; Lapointe, J.; Melati, D.; Cheben, P.; et al. Empirical model for the temperature dependence of silicon refractive index from O to C band based on waveguide measurements. Opt. Express 2019, 27, 27229–27241.

38 Padmaraju, Kishore, et al. "Wavelength locking and thermally stabilizing microring resonators using dithering signals." Journal of Lightwave Technology 32.3 (2013): 505-512.

39 Padmaraju, Kishore, et al. "Integrated thermal stabilization of a microring modulator." Optics express 21.12 (2013): 14342-14350.

40 Hassan, Ali H., et al. "A 0.002 ‐ mm2 8 ‐ bit 1 ‐ MS/s low ‐ power time ‐ based DAC (T ‐ DAC)." IET Circuits, Devices & Systems 15.8 (2021): 738-744.

41 Gan, Fuwan, et al. "Maximizing the thermo-optic tuning range of silicon photonic structures." 2007 Photonics in Switching. IEEE, 2007.

42 Amatya, Reja, et al. "Low power thermal tuning of second-order microring resonators." Conference on Lasers and Electro-Optics. Optica Publishing Group, 2007.